

## 2 **Changes in Crack Shape and Saturation in Laboratory-Induced Seismicity by Water** 3 **Infiltration in the Transversely Isotropic Case with Vertical Cracks**

5 **Koji Masuda<sup>1</sup>**

6 <sup>1</sup>Geological Survey of Japan, National Institute of Advanced Industrial Science and Technology,  
7 Tsukuba 305-8567, Japan

9 Corresponding author: Koji Masuda ([koji.masuda@aist.go.jp](mailto:koji.masuda@aist.go.jp))

### 11 **Key Points:**

- 12 • A laboratory method for estimating crack aspect ratio and degree of saturation based on a  
13 transversely isotropic solid model is presented.
- 14 • A water injection experiment with a stressed rock was conducted in which wave  
15 velocities; strain; and acoustic emission were measured.
- 16 • During injection of water to induce failure, the crack aspect ratio changed from 1/400 to  
17 1/160 and saturation increased from 0 to 0.6.

## 20 **Abstract**

21 Open cracks and cavities play important roles in fluid transport. Underground water penetration  
22 induces microcrack activity, which can lead to rock failure and earthquake. Fluids in cracks can  
23 affect earthquake generation mechanisms through physical and physicochemical effects.  
24 Methods for characterizing the crack shape and water saturation of underground rock are needed  
25 for many scientific and industrial applications. The ability to estimate the status of cracks by  
26 using readily observable data such as elastic-wave velocities would be beneficial. We have  
27 demonstrated a laboratory method for estimating the crack status inside a cylindrical rock sample  
28 based on a vertically cracked transversely isotropic solid model by using measured P- and S-  
29 wave velocities and porosity derived from strain data. During injection of water to induce failure  
30 of a stressed rock sample, the crack aspect ratio changed from 1/400 to 1/160 and the degree of  
31 water saturation increased from 0 to 0.6. This laboratory-derived method can be applied to well-  
32 planned observations in field experiments. The in situ monitoring of cracks in rock is useful for  
33 industrial and scientific applications such as the sequestration of carbon dioxide and other waste,  
34 induced seismicity, and measuring the regional stress field.

35

## 36 **Plain Language Summary**

37 When fluids such as water infiltrate underground they sometimes induce earthquakes, which can  
38 have disastrous results. In the process that causes this kind of induced seismicity, water affects  
39 the shape of the cavities that serve as underground water pathways. These cavities are closely  
40 related to earthquake generation mechanisms. To characterize this process, we need to determine  
41 the change in the shape of underground cavities based on observable data such as earthquake  
42 wave velocities. Here we present a method for estimating the shape and degree of water  
43 saturation of underground cavities and their change over time based on data from laboratory rock  
44 experiments. As water infiltrates, cavities flatten and the degree of water saturation can be  
45 estimated. A laboratory-derived method can be applied to well-planned observations in field  
46 experiments. In situ monitoring of underground conditions can be useful for industrial and  
47 scientific applications such as sequestration of carbon dioxide and other waste, induced  
48 seismicity, and measuring the regional stress field.

49

## 50 **1 Introduction**

51 Pore pressure change and fluid migration are known to cause rock deformation and failure (e.g.,  
52 Healy et al., 1968; Lei et al., 2008; Ohtake, 1987; Prioul et al., 2000; Raleigh et al., 1976).  
53 Because open cracks and cavities play important roles in fluid transport (Caine et al., 1996;  
54 Rutqvist et al., 2008), the evolution of microcracking in the presence of underground fluids and  
55 crustal stresses is a critical factor in geothermal energy extraction (e.g., Fehler, 1989), carbon  
56 dioxide capture and storage (e.g., Baines & Worden, 2004; Hangx et al., 2010), waste disposal,  
57 and induced seismicity (Ellsworth et al., 2013; Schultz et al., 2020). Methods to measure the  
58 volume and shape of cavities and cracks would be of great assistance in planning industrial and  
59 scientific applications, including characterization of regional stress fields and sequestration of  
60 carbon dioxide and other waste. Methods are particularly needed for in situ monitoring  
61 microcrack evolution at depths of around 1 km.

62

63 In this research on microcrack activity caused by hydrological effects inside rock samples, we  
64 conducted laboratory studies with the aim of constructing a basic model for these underground  
65 processes. This paper describes an in situ monitoring method for estimating the crack shape and  
66 degree of water saturation in rock samples from measured P- and S-wave velocities and porosity  
67 changes.  
68

69 Field experiments on water-induced seismicity have been conducted for scientific and industrial  
70 purposes. Experiments conducted in Matsushiro, Japan (Ohtake, 1987), and Rangely, Colorado,  
71 USA (Raleigh et al., 1976), have revealed relationships between water injection and induced  
72 microearthquakes. Water-injection experiments conducted in deep boreholes, such as the  
73 German Continental Deep Drilling Program (KTB), have revealed characteristics of induced  
74 seismicity (Jost et al., 1998; Zoback & Harjes, 1997). Other studies have examined  
75 microearthquakes induced by water injection to infer seismic mechanisms and movements of  
76 fluids (e.g., Eyre et al., 2019, 2020; Lei et al., 2008; Prioul et al., 2000; Schultz et al., 2017,  
77 2018; Wang et al., 2020). Such studies yield information on the relationship between water  
78 injection and initiation of microcracking; however, it is hard to obtain sufficient information  
79 about crack shape and degree of water saturation for modeling underground crack and fracture  
80 systems. Because of the difficulty of determining crustal stresses underground and distributing  
81 observation stations optimally, it is difficult to construct basic models using field studies.  
82

83 To investigate the shape of microcracks induced in rock samples, we studied hydromechanical  
84 effects on the complex processes that control rock failure in the laboratory. Laboratory studies  
85 enable us to tightly control conditions and precisely measure data such as sample deformation  
86 and velocity changes in P and S waves. Laboratory studies are useful for constructing physical  
87 models for basic mechanisms that take place in long-term geological processes (Benson et al.,  
88 2008; Burlini et al., 2009; Masuda, 2013; Masuda et al., 2012). For example, Kranz et al. (1990),  
89 Lockner and Byerlee (1977), Masuda et al. (1990), Lockner et al. (1991), and Scholz (1968)  
90 investigated microfracturing through acoustic emission (AE) inside rock samples and developed  
91 techniques for analyzing AE. The relationship between water migration and induced  
92 microfractures also has been investigated in the laboratory (e.g., Masuda et al., 1990, 1993;  
93 Stanchits et al., 2011).  
94

95 In this study, we developed a procedure for estimating crack status inside a rock sample based on  
96 a vertically cracked transversely isotropic solid model. We estimated two crack characteristics,  
97 crack shape and the degree of water saturation, and their changes during water migration into a  
98 granitic rock subjected to confining pressure and differential stress.  
99

## 100 **2 Sample and Methods**

101 A cylinder (50 mm in diameter and 100 mm in length) of medium-grained Inada granite with an  
102 average grain size of 5 to 6 mm was used for the experiment. A differential stress of 370 MPa,  
103 which corresponds to about 70% of fracture strength, was applied to the rock sample in the axial  
104 direction at a constant rate of 0.06 MPa/s under 30 MPa confining pressure and was held  
105 constant throughout the experiment. When the primary creep stage and AE caused by the initial  
106 loading had ceased, we injected distilled water into the bottom end of the sample at a constant

107 pressure of 25 MPa until macroscopic fracture occurred. Figure 1 shows the stress conditions and  
 108 the number of AE events as a function of time.

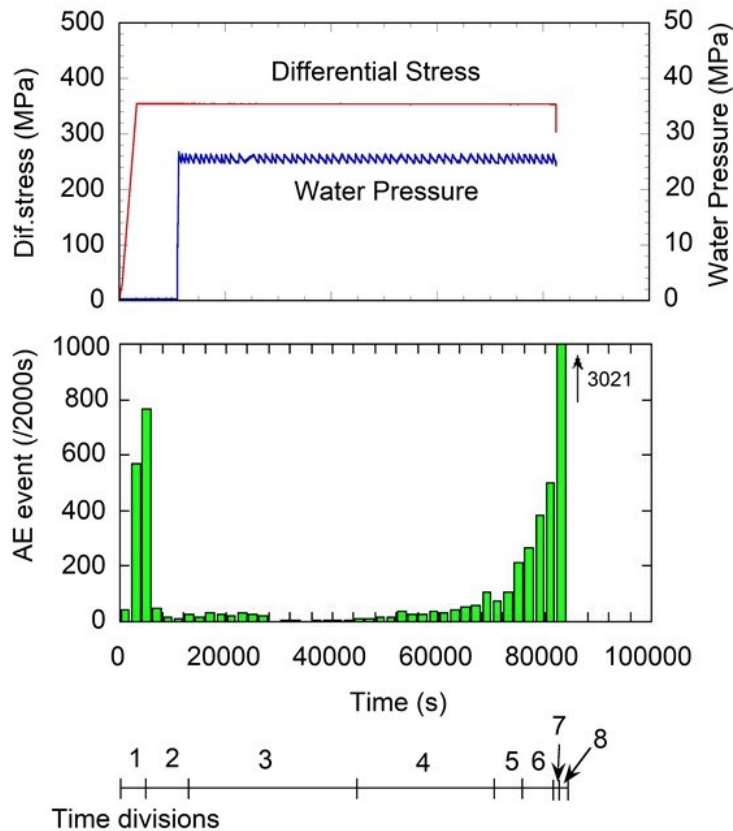


Figure 1

109  
 110 **Figure 1.** Changes in differential stress, water pressure at the injection site, and number of  
 111 acoustic emission (AE) events as a function of time. Confining pressure was 30 MPa. Numbers  
 112 at the bottom of the figure show time divisions for the plot of AE locations in Figure 8.  
 113

114

115 During water migration, P- and S-wave velocities, which propagated along five paths parallel to  
 116 the top and bottom surfaces of the sample, were measured. Strains of the sample surface and AE  
 117 were monitored and recorded. The locations of instrumentation on the surface of the rock sample  
 118 are shown in Figure 2. Axial and circumferential strains were measured using six pairs of strain  
 119 gauges at the midpoint of the sample's length as indicated by the large blue circles in Figure 2.  
 120 Piezoelectric transducers (PZTs) with 2-MHz resonant frequency were attached at the 18 places  
 121 indicated by the small red circles in Figure 2 and inside the top and the bottom end-pieces. At 10  
 122 of these locations (1–5 and 10–14 in Figure 2), we attached transducers for P waves, vertical S  
 123 waves ( $S_V$ ), and horizontal S waves ( $S_H$ ), in which the subscript specifies the direction of  
 124 vibration. With the pulse transmission method, P-wave and horizontal and vertical S-wave  
 125 velocities across the rock sample at five locations were measured (Figure 3). Because low-  
 126 porosity aggregate was considered, the effect of porosity on the density of the sample could be  
 127 ignored in calculating velocities (Anderson et al., 1974). In this study, the sample rock material  
 128 was considered to be homogeneous because the wavelength of the wave velocity was longer than

129 the scale length of heterogeneity in the rock. The sampling rate of the digital recording system  
 130 was 50 ns. AE signals were also recorded with all 18 P-wave transducers shown in Figure 2, plus  
 131 the two transducers on the top and bottom of the rock sample. AE hypocenters were determined  
 132 by the automatic arrival time and hypocenter determination method of Lei et al. (2004).

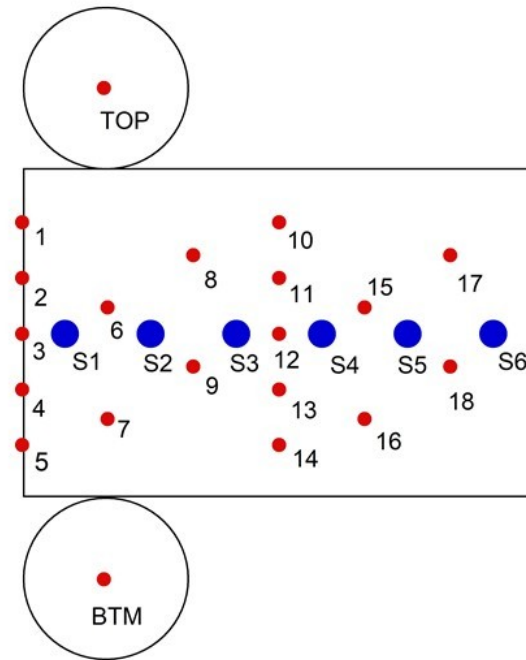


Figure 2

133  
 134 **Figure 2.** Locations of piezoelectric transducers and strain gauges on a rock sample. Schematic  
 135 map of the cylindrical surface of the sample. Large blue circles (S1 to S6) indicate the locations  
 136 of pairs of cross-strain gauges that monitored surface strains. Small red circles (1 to 18, TOP,  
 137 BTM) indicate the locations of piezoelectric transducers.  
 138

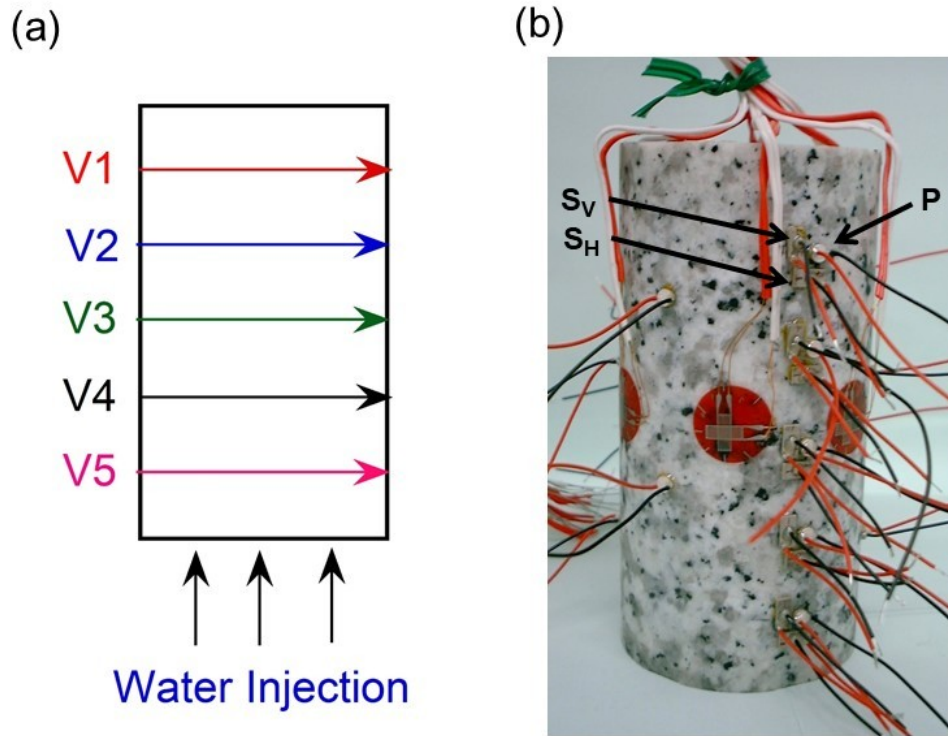


Figure 3

139 **Figure 3.** Paths of velocity measurements across the rock sample. (a) For P- and S-wave velocity  
 140 measurements, elastic pulses were initiated from transducers V1 through V5 (at locations 1  
 141 through 5 in Figure 2) and received by transducers on the other side (at locations 10 through 14  
 142 in Figure 2). Water was injected uniformly from the bottom surface of the rock sample. (b)  
 143 Photograph of the instrumented rock sample showing placement of transducers for detection of  
 144 three types of elastic waves (locations 1–5 and 10–14 in Figure 2).  
 145  
 146

147

148 After the experiment, X-ray computer tomography (CT) images of the rock sample were created.  
 149 Images were made in the plane perpendicular to the sample axis at 1-mm intervals, then  
 150 combined into a three-dimensional model displaying the internal structure of the sample,  
 151 including the shapes and locations of the fracture planes.  
 152

### 153 3 Results

#### 154 3.1. P-wave velocity

155 The measured P-wave velocities in the rock sample are shown in Figure 4 as a function of time.  
 156 During the initial loading stage, the P-wave velocity decreased due to the opening of new  
 157 microcracks. After water injection began, the P-wave velocity increased on each measurement  
 158 path in sequence from 5 to 1 as the water reached it (Figure 4) because open pores were partially  
 159 filled with water, a phenomenon well documented in the literature (e.g., Budiansky & O'Connell,

160 1976; O'Connell & Budiansky, 1974). The P-wave velocity then gradually decreased due to  
 161 undersaturation as the rate of cracking exceeded the rate of fluid flow, similar to the pattern  
 162 documented by Masuda et al. (1990, 1993).

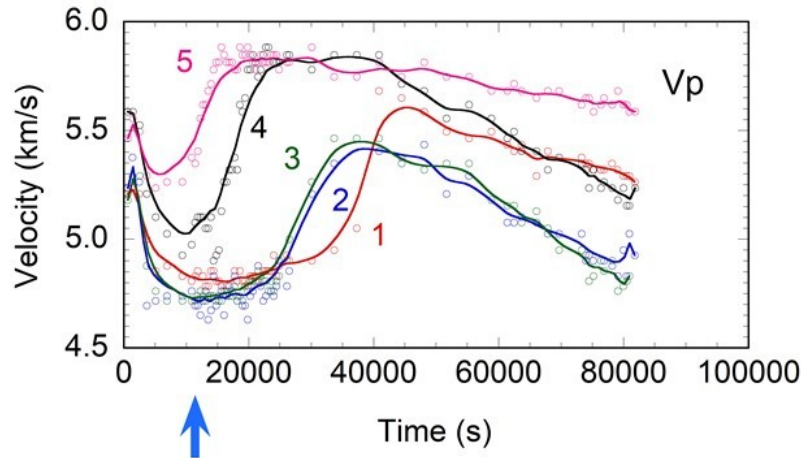


Figure 4

163 **Figure 4.** P-wave velocity for five transects of the rock sample (locations shown in Figure 3a) as  
 164 a function of time. The blue arrow indicates the time when water injection started (modified from  
 165 Masuda et al., 2013).  
 166  
 167

### 168 3.2. S-wave velocity

169 The velocities of the vertical and horizontal S waves are shown in Figure 5. Some transducers  
 170 failed and yielded no data for the vertical S waves in measurement path 4 and for the horizontal  
 171 S waves in paths 1, 3, and 4. At the times when the injected water front reached the measurement  
 172 paths, as estimated from the P-wave velocity changes, the S-wave velocities increased slightly  
 173 and then decreased gradually.  
 174  
 175

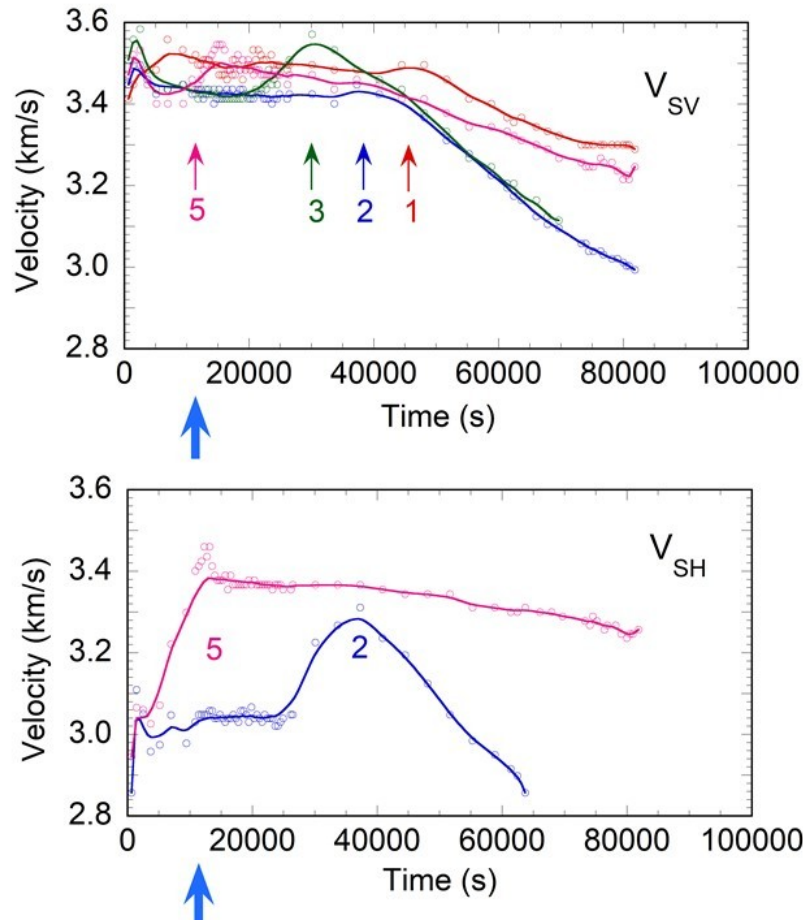


Figure 5

176

177 **Figure 5.** S-wave velocity with (a) vertical vibration  $S_V$  and (b) horizontal vibration  $S_H$  for four  
 178 transects of the rock sample (locations shown in Figure 3a) as a function of time. The blue arrow  
 179 indicates the time when water injection started. The numbered arrows show the estimated time  
 180 when the water front reached the corresponding measurement path. Velocity data for several  
 181 transects were not available.

182

183

184 The changes in  $V_p/V_s$  (where  $V_p$  and  $V_s$  are the P- and S-wave velocities, respectively) for  
 185 vertical and horizontal S waves are plotted in Figure 6. This ratio tends to be somewhat higher in  
 186 the absence of cracks, and saturating the cracks leads to an increase in  $V_p/V_s$  as described by  
 187 Paterson and Wong (2005).

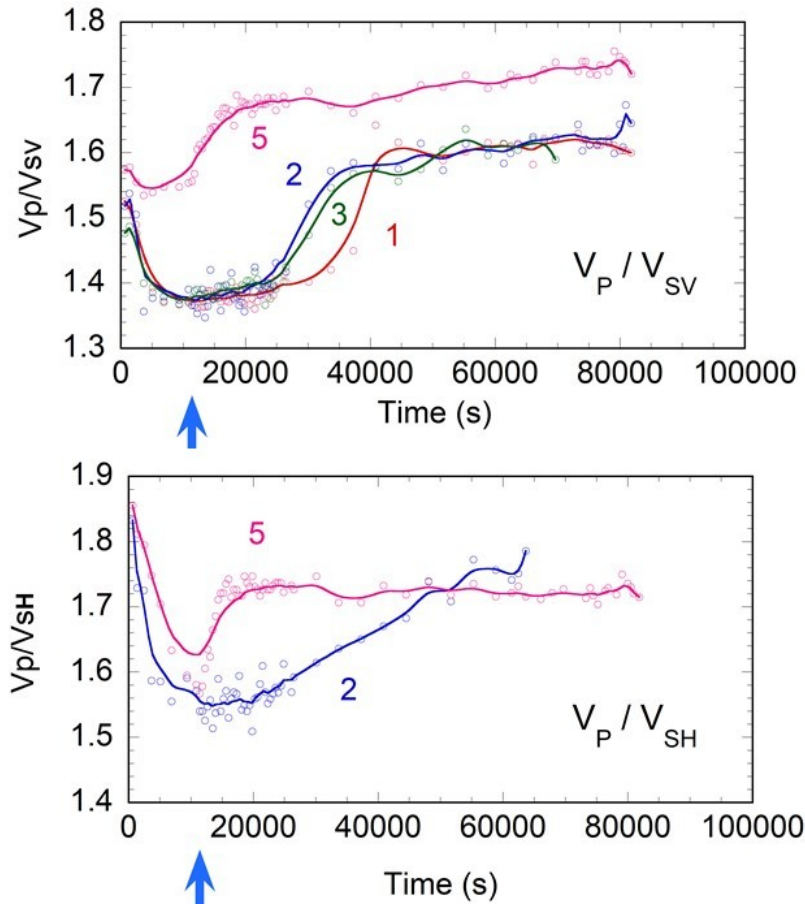


Figure 6

188

189 **Figure 6.**  $V_p/V_s$  ratios for  $S_V$  and  $S_H$  waves for transects of the rock sample (locations shown in  
 190 Figure 3a) as a function of time.

191

192

### 193 3.3 Strain

194 The average axial, circumferential, and volumetric strains measured at the midpoint of the  
 195 sample are shown in Figure 7. The strain gauges for axial strain at point S4 (Figure 2) failed, so  
 196 no data were available. The plotted axial strain data were averaged over the remaining five  
 197 locations. The circumferential strain shown is the average data for all six locations of the strain  
 198 gauges. The volumetric strain was calculated as the axial strain plus two times the  
 199 circumferential strain. After a time duration of 60,000 s, the circumferential strains measured at  
 200 locations S3 and S4 rapidly increased and the strain gauges at these locations failed.

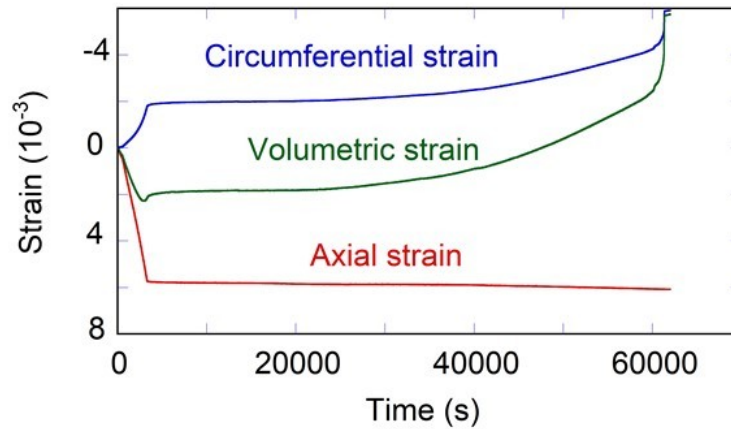


Figure 7

201  
202  
203  
204  
205

**Figure 7.** The average axial, circumferential, and volumetric strains as a function of experimental duration.

### 206 3.4. AE hypocenter distribution

207 AE hypocenters were calculated by automated detection of P-wave arrivals. Figure 8 shows  
208 stereographic projections of AE hypocenter distributions for the eight time periods shown in  
209 Figure 1. The estimated location error for most AE events was less than 2 mm (e.g., Lei et al.,  
210 2004; Schubnel et al., 2003). Clustering of AE events was not observed except just before the  
211 final fracture (periods 7 and 8). In the initial loading stage (period 1), AE was distributed evenly  
212 throughout the sample, suggesting that the loading was achieved uniformly. Before the start of  
213 water injection (period 2) and just afterward (period 3), AE activity decreased. In periods 3 and  
214 4, AE persisted in the middle of the sample and expanded upward, and in periods 5 and 6 AE  
215 activity increased. Just before the fracture (periods 7 and 8), AE clustered in the lower part at a  
216 location corresponding to the final fracture surface.

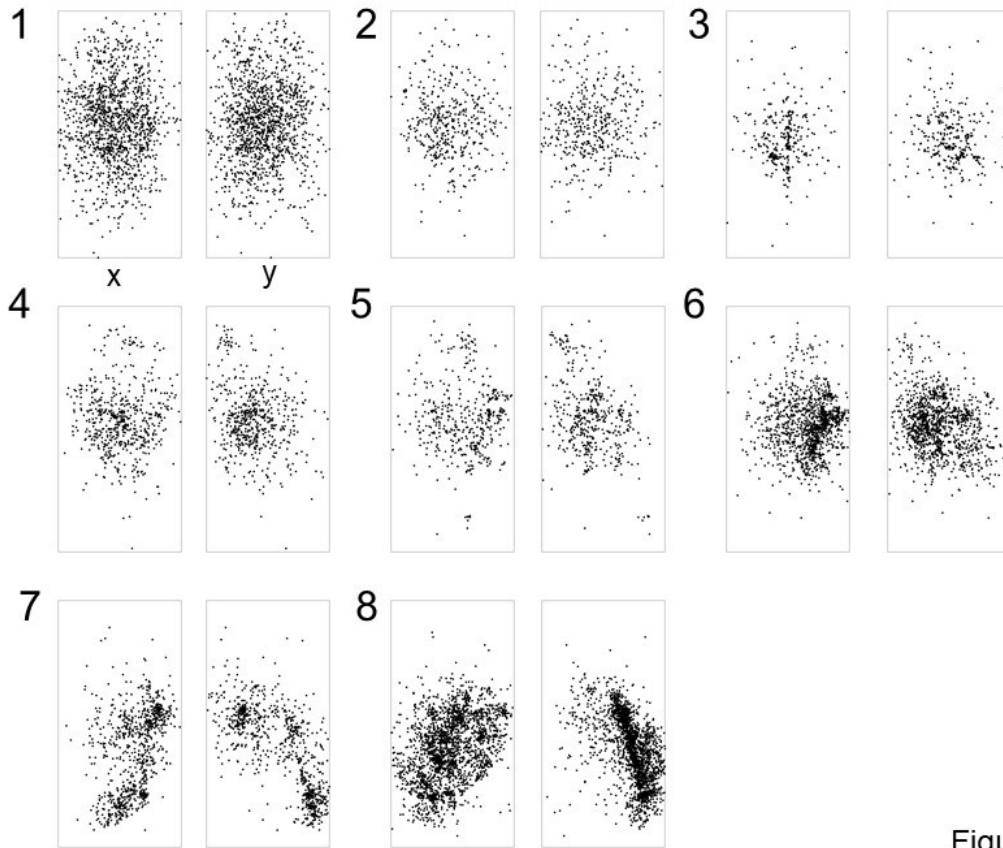


Figure 8

217  
218  
219  
220  
221

**Figure 8.** The vertical cross sections of the rock sample showing AE event locations during the eight time periods indicated in Figure 1.

### 222 3.5. X-ray CT imagery

223 After the experiment, we compiled 2D X-ray CT-images perpendicular to the sample axis, each  
224 representing 1 mm in thickness, at 1-mm intervals along the sample axis (99 total). The 3D  
225 image shown in Figure 9 was constructed from these 2D images. Figure 10 shows vertical cross  
226 sections derived from the 3D image. Three fracture surfaces (F1, F2, and F3) were recognized.  
227 The location and shape of surface F1 correspond to the fracture surface indicated by the AE  
228 hypocenter distributions (Figure 8). Fracture surface F2 formed at the edge of the sample,  
229 parallel to the sample surface. Fracture surface F3 was a small planar feature derived from the  
230 main rupture surface F1. The AE hypocenter distributions shown in Figure 8 indicate that rupture  
231 surface F1 formed and grew throughout the experiment whereas surfaces F2 and F3 formed just  
232 before the final fracture. According to microstructural studies by Moore and Lockner (1995),  
233 Paterson and Wong (2005), and Wong (1982), as the onset of marked localization of  
234 microcracking is approached, microcracks continue to be predominantly of axial orientation, but  
235 an increasing proportion are of inclined orientation or shear character.

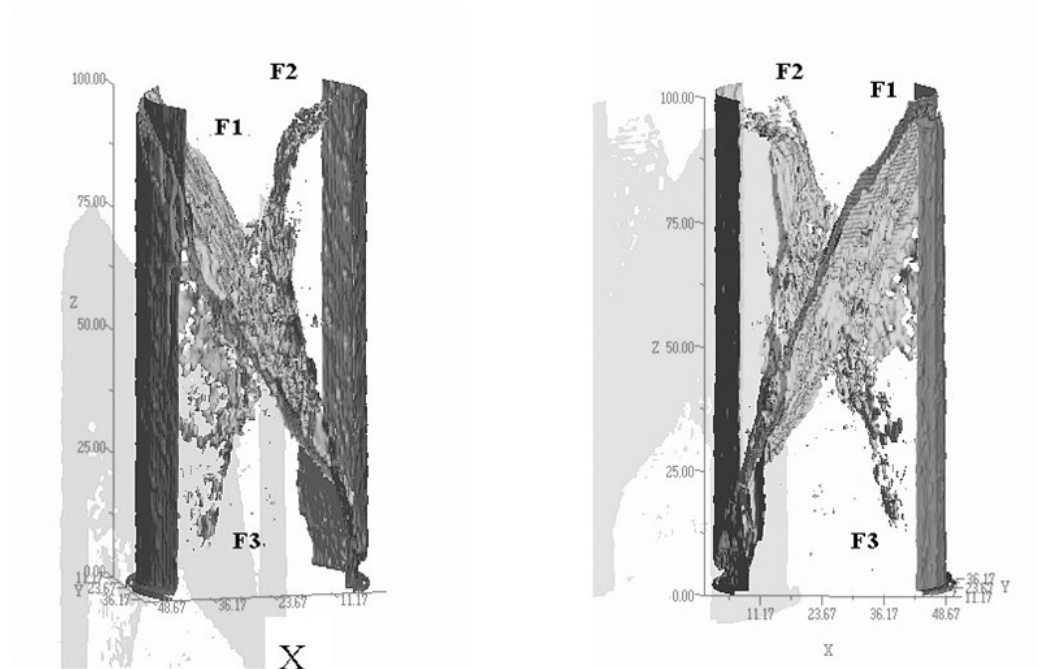


Figure 9

236  
 237  
 238  
 239  
 240  
 241

**Figure 9.** 3D CT image of the fracture planes (F1 through F3) of the sample from two viewpoints. The X-direction indicated in the left-hand image is the same as shown in Figure 10. The right-hand image is shown from the opposite side of the left-hand image. The offset gray shadowy images are visual aids.

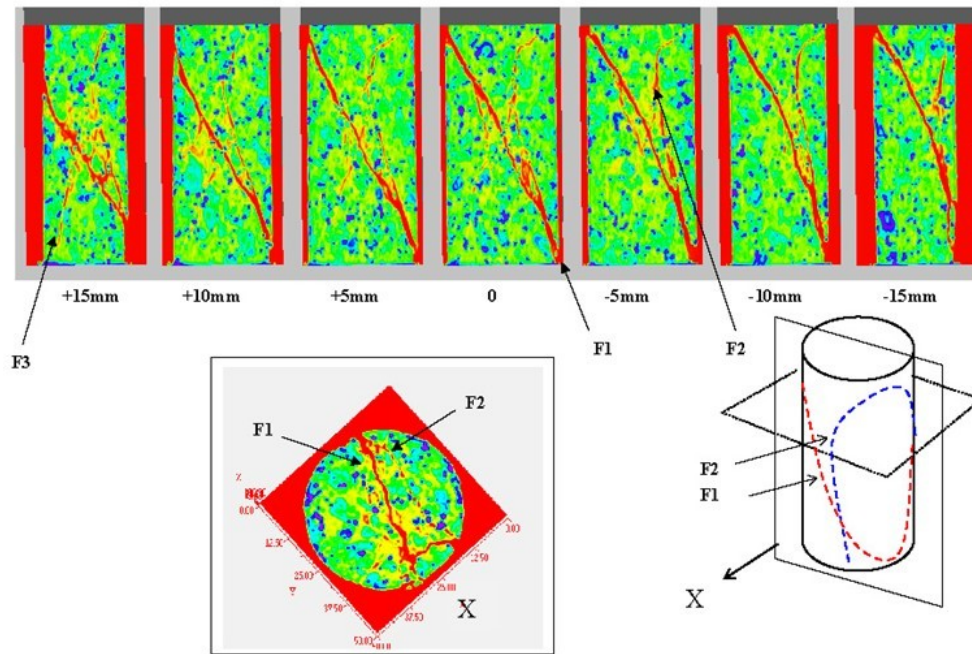


Figure 10

242  
 243 **Figure 10.** Horizontal CT cross section of the sample (65 mm from the sample base) after the  
 244 experiment and vertical 2D images derived from 3D CT model at intervals of 5 mm from the  
 245 center of the sample. Red color indicates low density. Progression from red to yellow, green, and  
 246 blue colors indicates increasing density. The X-direction indicated in the left-hand image is the  
 247 same as shown in Figure 9.

248  
 249

## 250 4 Discussion

### 251 4.1 Cracked solid model

252 We estimated crack parameters such as aspect ratio, the degree of water saturation, and their  
 253 changes as a function of time. In the evaluation of these parameters, a cracked solid model (e.g.,  
 254 Crampin, 1978, 1984; Hudson, 1981; Nishizawa & Masuda, 1991; Soga et al., 1978) that  
 255 approximates the rock as an elastic solid containing cavities representing pore space was applied.  
 256 Because cavities are more compliant than solid material, they have the effect of reducing the  
 257 elastic stiffness of the rock (e.g., Avseth et al., 2005; Mavko et al., 2009; Meglis et al., 1996).  
 258

259 In this study, we assumed a transversely isotropic medium in which vertical cracks of ellipsoidal,  
 260 penny-shaped geometry distributed with the orientations of the crack normals randomly  
 261 distributed in the plane perpendicular to the maximum stress as described in the Supporting  
 262 Information (Figures S1 and S2) (e.g., Fossen, 2010; Scholz, 2002). Transverse isotropy is

263 considered to be realistic when we consider seismic wave propagation in the Earth's crust. If this  
 264 is the case, the velocities of S waves that propagate horizontally would be affected differently, as  
 265 is seen in Figure 11; this effect is referred to as shear wave splitting (e.g., Anderson et al., 1974;  
 266 Paterson & Wong, 2005). Figure 11 shows that the velocities of S waves with horizontal  
 267 vibration are reduced more than those with vertical vibration for the data measured on both paths  
 268 2 and 5. The differences between  $V_{SV}$  and  $V_{SH}$  are larger for the data measured on path 2. This is  
 269 because path 2 is near the center of the sample, whereas path 5 is close to the end of the sample  
 270 where the crack volume is smaller than it is in the center. All of these observations support the  
 271 use of a vertically cracked transversely isotropic model in this study.

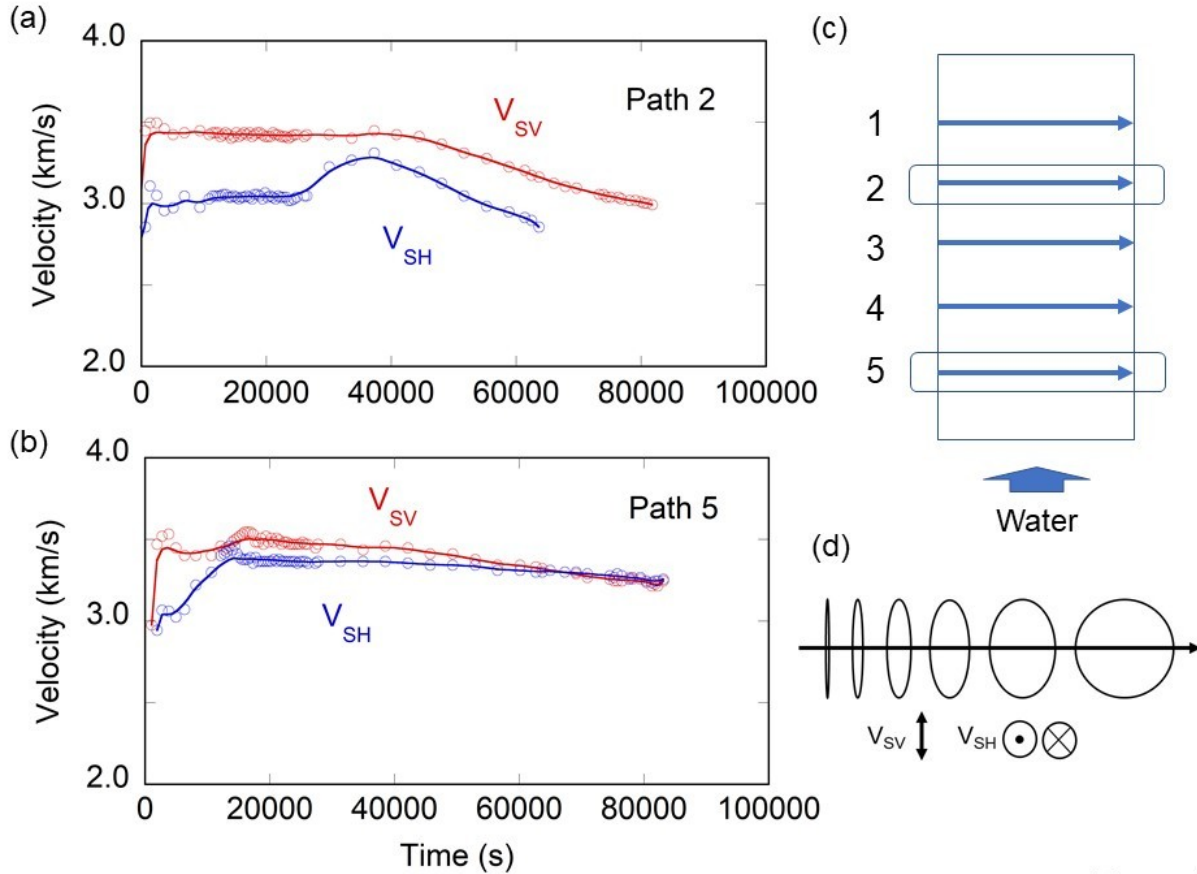


Figure 11

272 **Figure 11.** S-wave velocity with vertical vibration  $S_V$  and horizontal vibration  $S_H$  for (a) path 2  
 273 and (b) path 5. (c) Paths of the velocity measurements. (d) The wave propagation direction (thick  
 274 blue arrow) and side view of the crack distribution in the transversely isotropic model with  
 275 vertical cracks. The directions of vibration of the  $S_V$  and  $S_H$  waves are shown. Shear wave  
 276 splitting was observed, supporting the assumption of transversely isotropic symmetry with  
 277 vertical crack distribution.  
 278  
 279  
 280

281 The change in elastic wave velocities during the experiment was attributed to open cracks in the  
 282 rock sample. The effect of cracks on the elastic properties of solids depends on various factors  
 283 such as the shape, number, and orientation of the cracks. When very thin spheroidal cracks are

284 randomly distributed in a solid, O'Connell and Budiansky (1974) showed that the effect of  
 285 cracks on velocity is well described by the crack density parameter,  
 286

$$\varepsilon = N \langle a^3 \rangle = \frac{3}{4\pi} \frac{\phi}{\alpha}, \quad (1)$$

287  
288

289 where  $\langle a \rangle$  is the mean major axis of the crack ellipsoid;  $N$  is the number of cracks per unit  
 290 volume of the solid;  $\phi$  is the volume of cracks per unit volume of the solid, which can be written  
 291 as  
 292

$$\phi = \frac{4}{3} \pi \langle a^2 c \rangle N; \quad (2)$$

293  
294

295 and  $\alpha$  is the aspect ratio of a very thin spheroidal crack ( $a = b \gg c$ ),  $\alpha = c/a$ . According to  
 296 Hudson (1981) and Soga et al. (1978), the effect of cracks on velocity, in terms of the ratio of  
 297 velocities with and without cracks, is proportional to the crack density parameter  $\varepsilon$  at small  
 298 values of  $\varepsilon$ ,  
 299

$$(V/V_0)^2 = 1 - p_i \varepsilon, \quad (3)$$

300  
301

302 where  $V_0$  and  $V$  are the elastic wave velocities of the rocks without and with cracks, respectively.  
 303 The constants  $p_i$  can be calculated for P waves and two kinds of S waves under dry and saturated  
 304 states (Table 1). Details regarding how to calculate the coefficients listed in Table 1 are  
 305 described in the Supporting Information.  
 306

307 **Table 1.** The right sides of equation (3) with the constants  $p_i$  for dry and wet states. Details  
 308 regarding the determination of the constants  $p_i$  are described in the Supporting Informantion.  
 309

	$V_p$	$V_{SV}$	$V_{SH}$
Dry	$1 - \frac{71}{21} \varepsilon$	$1 - \frac{8}{7} \varepsilon$	$1 - \frac{15}{7} \varepsilon$
Wet	$1 - \frac{8}{21} \varepsilon$	$1 - \frac{8}{7} \varepsilon$	$1 - \frac{8}{7} \varepsilon$

310  
311  
312

313 In partially saturated cases, P- and S-wave velocities can be interpolated from the dry and wet  
 314 (saturated) velocities by using the degree of water saturation parameter  $\xi$ , which ranges from 0  
 315 (dry) to 1.0 (saturated). In this study, it is assumed that elastic constants in the partially saturated  
 316 state can be expressed as the weighted average of the elastic constants of dry and saturated states  
 317 (Voigt's average). Then the velocity  $V$  of a partially saturated state can be written as  
 318

$$V^2 = \xi V_w^2 + (1 - \xi) V_d^2, \quad (4)$$

319

320

321 where  $V_w$  and  $V_d$  are the velocities for the totally saturated and totally dry cases, respectively.  
 322 From equations (1) through (4), equation (3) can be rewritten as

323

$$1 - \left( \frac{V_{p,s}}{V_0} \right)^2 = p_i \frac{3}{4\pi} \frac{\phi}{\alpha} \quad (5)$$

324

325

326 Here  $V_p$  and  $V_s$  are the P- and S-wave velocities for rocks that include cracks. The total crack  
 327 volume ratio  $\phi$  is calculated by using the measured surface strains of the rock sample as shown in  
 328 the following section. Thus, given a set of  $\alpha$  and  $\xi$  values, we can calculate curves of  $1 - (V/V_0)^2$   
 329 versus  $\phi$  for P and S waves. By comparing the calculated curves to the measured data shown in  
 330 Figure 12, we estimate  $\alpha$  and  $\xi$  and their variation with time by fitting for each measured  
 331 experimental data set.

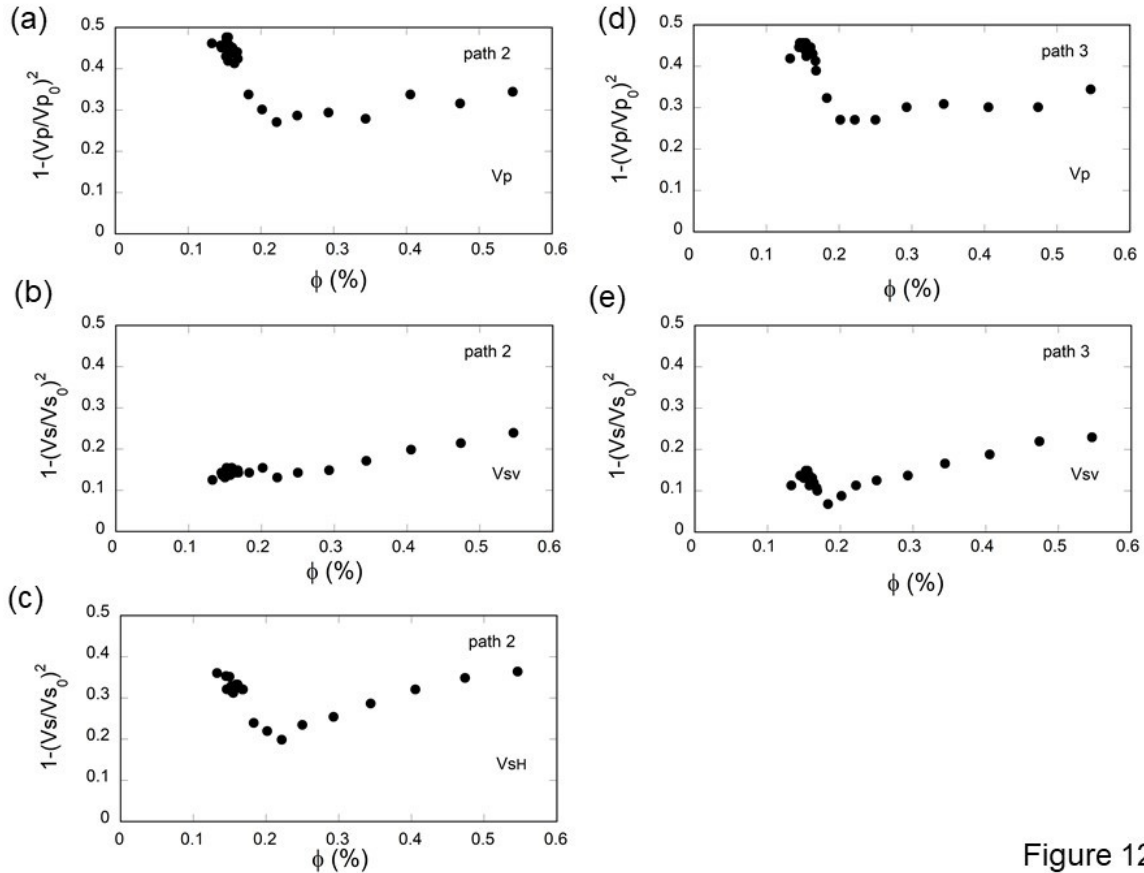


Figure 12

332

333 **Figure 12.** Measured data plotted for  $\phi$  vs.  $1 - (V/V_0)^2$ . (a)  $V_p$ , (b)  $V_{sV}$ , (c)  $V_{sH}$  for path 2, and  
 334 (d)  $V_p$ , (e)  $V_{sV}$  for path 3.

335

336

#### 337 4.2. Change in crack shape and degree of water saturation

338 Figure 13 shows the P-wave velocity change  $1 - (V_p/V_{p0})^2$  as a function of  $\phi$ , the volume of  
 339 cracks per unit volume of the solid. We calculated  $\phi$  based on strain data measured at the center

340 of the rock sample (Figures 2 and 7). We first calculated the volumetric strain  $\varepsilon_v$  from the  
 341 averages of the axial strain  $\varepsilon_z$  and circumferential strain  $\varepsilon_\theta$  as  $\varepsilon_v = \varepsilon_z + 2\varepsilon_\theta$ . The stress–strain  
 342 curve was linear in the early stage of loading except for the initial stage. Taking the linear part of  
 343 the volumetric strain to represent the elastic volumetric strain, we fitted the  $\varepsilon_v$  versus stress line  
 344 in the range from 1/9 to 1/3 of the failure stress by a straight line using the least-squares method.  
 345 This stress range was used to avoid the effects of initial cracks at low stress levels and new  
 346 cracks at high stress levels. We then calculated the dilatant strain  $\varepsilon_{dv}$  from the observed  
 347 volumetric strain by subtracting the elastic volumetric strain predicted by the straight line (e.g.,  
 348 Brace et al., 1966; Paterson & Wong, 2005). We then used the calculated dilatant strain to  
 349 represent  $\phi$ . Here we used the P- and S-wave velocity data measured along paths V2 and V3 at  
 350 the midpoint of the sample (Figure 3). Figure 13 shows that the curve of  $\alpha = 1/400$  and  $\xi = 0$  is  
 351 best fitted to the data indicated by the arrow. Thus we estimated that the aspect ratio of the  
 352 cracks before water injection (in the dry state,  $\xi = 0$ ) was 1/400.

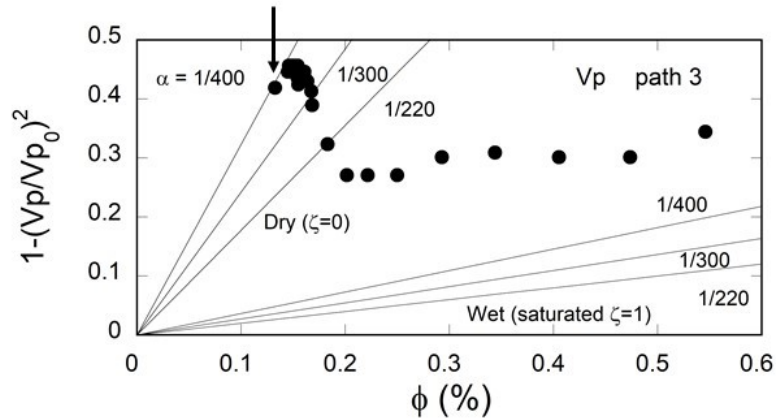


Figure 13

353  
 354 **Figure 13.** Procedure for estimating the pair of values for the crack aspect ratio and water  
 355 saturation ( $\alpha$ ,  $\xi$ ) for the case of  $\xi = 0$ . Values of  $1 - (V_p/V_{p_0})^2$  as a function of crack volume  $\phi$  are  
 356 plotted for  $V_p$  measured on path 3. Curves are shown for three values of  $\alpha$  and endpoint values  
 357 (0 and 1) of  $\xi$ . The data point indicated by the arrow, which was measured at the beginning of the  
 358 velocity measurement, is nearly on the curve for the ( $\alpha$ ,  $\xi$ ) pair (1/400, 0). Curves for the  
 359 saturated case ( $\xi = 1$ ) are shown as references.

360  
 361

362 To estimate  $\alpha$  and  $\xi$  simultaneously after water injection for the case of  $\xi > 0$ , we need more than  
 363 two kinds of data, such as  $V_p$ ,  $V_{Sv}$ , or  $V_{Sh}$ . The best fitted set of  $(\alpha, \xi)$  to the measured data was  
 364 estimated by the grid search method using equations (4) and (5) with the constants  $p_i$  listed in  
 365 Table 1. For example, Figure 14 shows the curves of  $\alpha = 1/160$  with  $\xi = 0, 0.2, 0.4, 0.6, 0.8,$  and  
 366 1.0 for  $V_p$  and  $\xi = 0.6$  with  $\alpha = 1/200, 1/180, 1/160, 1/140, 1/120,$  and  $1/100$  for  $V_{Sv}$  for path 3.  
 367 For the last data point plotted, around  $\phi = 0.55$ , our best fitted set of  $(\alpha, \xi)$  was  $\alpha = 1/160$  and  $\xi =$   
 368 0.6.

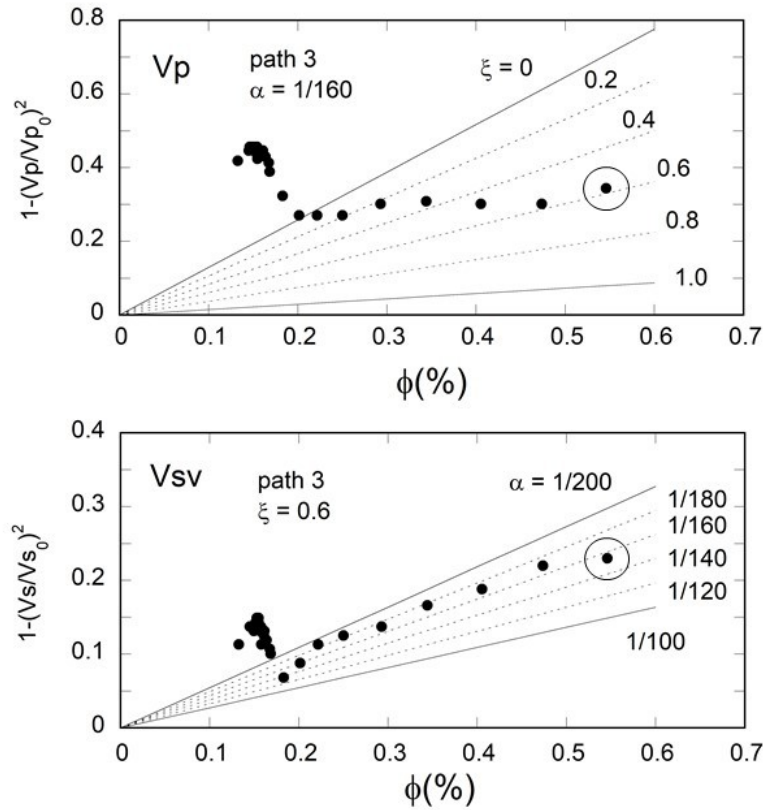


Figure 14

369 **Figure 14.**  $1-(V/V_0)^2$  as a function of  $\phi$  for  $V_p$  with curves for  $\alpha = 1/160$  and six values of  $\xi$ , and  
 370 for  $V_{Sv}$  with curves for  $\xi = 0.6$  and six values of  $\alpha$ .  $V_p$  and  $V_{Sv}$  data were used to simultaneously  
 371 estimate a pair of values for the crack aspect ratio and water saturation  $(\alpha, \xi)$ . The last data point  
 372 indicated by the circle, at about  $\phi = 0.55$ , was best fit by the set of  $\alpha = 1/160$  and  $\xi = 0.6$ .  
 373  
 374  
 375

376 Figure 15 shows the estimated crack aspect ratio  $\alpha$  and degree of water saturation  $\xi$  as a  
 377 function of time. The aspect ratio changed from  $1/400$  to about  $1/160$  during the deformation as a  
 378 result of water injection. Water saturation in the middle of the sample increased from 0 to 0.6.  
 379

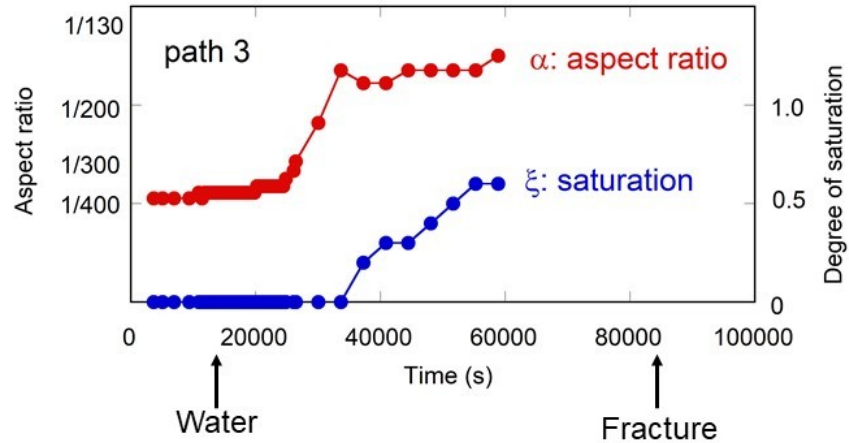


Figure 15

380 **Figure 15.** Changes in the aspect ratio (red) and water saturation (blue) at the midpoint of the  
 381 sample as a function of time. The arrows labeled “Water” and “Fracture” mark the times when  
 382 water injection started and when the rock sample fractured, respectively.  
 383  
 384  
 385

## 386 5 Conclusions

387 We demonstrated an in situ monitoring method for estimating crack shape and degree of water  
 388 saturation from measured P- and S-wave velocities and porosity changes in the laboratory. We  
 389 fractured an instrumented rock sample by injecting it with water under well-controlled  
 390 differential stress and confining pressure conditions. We estimated the crack aspect ratio and the  
 391 degree of water saturation by applying a cracked solid model to our experimental data on P- and  
 392 S-wave velocities and crack density. We observed that (1) the aspect ratio  $\alpha$  of dry cracks before  
 393 water injection was 1/400, (2) during the water migration the aspect ratio changed from 1/400 to  
 394 1/160, and (3) the degree of water saturation  $\xi$  increased from 0 to 0.6. The monitoring methods  
 395 described in this study may be useful in the estimation of microcracking at depth. Reliable  
 396 monitoring methods for detecting crack characteristics and their time variation will aid in  
 397 planning industrial and scientific applications including measurement of regional stress fields,  
 398 induced seismicity, and sequestration of carbon dioxide and other waste.

### 399 **Acknowledgments, Samples, and Data**

400 The author declares no financial conflict of interests.

401

402 The original velocity, strain, and AE data used in this work will be uploaded to a public  
403 repository Zenodo once accepted. Data are currently available on my institution's webpage as  
404 <https://staff.aist.go.jp/koji.masuda/seika/data/JGR2021.html> for review purposes.

405

406 This work was supported by the general funding of the Geological Survey of Japan, AIST.

407

408 T. Maruyama of the University of Tsukuba contributed to the experimental study. O. Nishizawa  
409 and X. Lei of the Geological Survey of Japan contributed to the data manipulation.

410

411

### 412 **References**

413 Anderson, D. L., Minster, B., & Cole, D. (1974). The effect of oriented cracks on seismic

414 velocities. *Journal of Geophysical Research*, 79(26), 4011-4015, DOI:

415 <https://doi.org/10.1029/JB079i026p04011>

416 Avseth, P., Mukerji, T., & Mavko, G. (2005). *Quantitative seismic interpretation,*

417 *Applying rock physics tools to reduce interpretation risk*, UK: Cambridge Univ. Press.

418 Baines, S. J., & Worden, R. H. (Eds.) (2004). *Geological Storage of Carbon Dioxide,*

419 *Special Publications*, 233, London: Geological Society.

420 Benson, P. M., Vinciguerra, S., Meredith, P. G., & Young R. P. (2008). Laboratory

421 simulation of volcano seismicity, *Science*, 322, 249-252, DOI: 10.1126/science.1161927

422 Brace, W., Paulding, B., & Scholz, C. (1966). Dilatancy in the Fracture of Crystalline

423 Rocks, *Journal of Geophysical Research*, 71, 16, doi:10.1029/JZ071i016p03939

424 Budiansky, B., & O'Connell, R. J. (1976). Elastic moduli of a cracked solid, *International*

425 *Journal of Solids and Structures*, 12, 81-97, <http://dx.doi.org/10.1016/0020->

426 7683(76)90044-5

427 Burlini, L., Di Toro, G., & Meredith, P. (2009). Seismic tremor in subduction zones:

428 Rock physics evidence, *Geophysical Research Letters*, 36, L08305,

429 doi:10.1029/2009GL037735

430 Caine, J. S., Evans, J. P., & Forster, C. B. (1996). Fault zone architecture and

431 permeability structure, *Geology*, 24, 1025-1028, doi:10.1130/0091-7613 (1996)

432 024<1025:FZAAPS>2.3.CO;2

433 Crampin, S. (1978). Seismic wave propagation through a cracked solid: Polarization as

434 a possible dilatancy diagnostic, *Geophysical Journal of the Royal Astronomical Society*,

435 53, 467-496, DOI: 10.1111/j.1365-246X.1978.tb03754.x

436 Crampin, S. (1984). Effective anisotropic elastic constants for wave propagation

437 through cracked solids, *Geophysical Journal of the Royal Astronomical Society*, 76,

438 135-145, DOI: 10.1111/j.1365-246X.1984.tb05029.x

439 Ellsworth, W. L. (2013). Injection-Induced Earthquakes. *Science* 341, 1225942.

440 DOI: 10.1126/science.1225942

441 Eyre, T. S., Eaton, D. W., Garagash, D. I., Zecevic, M., Venieri, M., Weir, R., & Lawton, D. C.

442 (2019). The role of aseismic slip in hydraulic fracturing-induced seismicity. *Science*

443 *Advances*, 5(8), eaav7172. DOI: 10.1126/sciadv.aav7172

- 444 Eyre, T. S., Zecevic, M., Salvage, R. O., & Eaton, D. W. (2020). A long-lived swarm of  
445 hydraulic fracturing-induced seismicity provides evidence for aseismic slip, *Bulletin of*  
446 *the Seismological Society of America*, 110, 2205–2215. doi: 10.1785/0120200107
- 447 Fehler, M. C. (1989), Stress control of seismicity patterns observed during hydraulic  
448 fracturing experiments at the Fenton Hill hot dry rock geothermal energy site, New  
449 Mexico, *International Journal of Rock Mechanics and Mining Sciences &*  
450 *Geomechanics Abstracts*, 26, 211-219, [http://dx.doi.org/10.1016/0148-9062\(89\)91971-2](http://dx.doi.org/10.1016/0148-9062(89)91971-2)
- 451 Fossen, H. (2010), *Structural Geology*, UK: Cambridge Univ. Press.
- 452 Hangx, S. J. T., Spiers, C. J., & Peach, C. J. (2010). Mechanical behavior of anhydrite  
453 caprock and implications for CO<sub>2</sub> sealing capacity, *Journal of Geophysical Research*,  
454 115, B07402, doi:10.1029/2009JB006954
- 455 Healy, J. H., Rubey, W. W., Griggs, D. T., & Raleigh, C. B. (1968). The Denver  
456 earthquakes, *Science*, 161, 1301-1310, doi:10.1126/science.161.3848.1301
- 457 Hudson, J. A. (1981). Wave speeds and attenuation of elastic waves in material  
458 containing cracks, *Geophysical Journal of the Royal Astronomical Society*, 64, 133-150,  
459 DOI: 10.1111/j.1365-246X.1981.tb02662.x
- 460 Jost, M. L., Bübelberg, T., Jost, Ö., & Harjes, H.-P. (1998) Source parameters of  
461 injection-induced microearthquakes at 9 km depth at the KTB deep drilling site,  
462 Germany, *Bulletin of the Seismological Society of America*, 88, 815-832
- 463 Kranz, R. L., Satoh, T., Nishizawa, O., Kusunose, K., Takahashi, M., Masuda, K., &  
464 Hirata, A. (1990). Laboratory study of fluid pressure diffusion in rock using acoustic  
465 emissions, *Journal of Geophysical Research*, 95(B13), 21,593–21,607,  
466 doi:10.1029/JB095iB13p21593
- 467 Lei, X., Masuda, K., Nishizawa, O., Jouniaux, L., Liu, L., Ma, W., Satoh, T., & Kusunose,  
468 K. (2004). Detailed analysis of acoustic emission activity during catastrophic fracture of  
469 faults in rock, *Journal of Structural Geology*, 26, 247–258,  
470 [http://dx.doi.org/10.1016/S0191-8141\(03\)00095-6](http://dx.doi.org/10.1016/S0191-8141(03)00095-6)
- 471 Lei, X., Yu, G., Ma, S., Wen, X., & Wang, Q. (2008). Earthquakes induced by water  
472 injection at ~3 km depth within the Rongchang gas field, Chongqing, China, *Journal of*  
473 *Geophysical Research*, 113, B10310, doi:10.1029/2008JB005604
- 474 Lockner, D., & Byerlee, J. D. (1977). Hydrofracture in Weber sandstone at high  
475 confining pressure and differential stress, *Journal of Geophysical Research*, 82(14),  
476 2018–2026, doi:10.1029/JB082i014p02018
- 477 Lockner, D. A., Byerlee, J. D., Kuksenko, V., Ponomarev, A., & Sidorin, A. (1991).  
478 Quasi-static fault growth and shear fracture energy in granite, *Nature*, 350, 39-42,  
479 doi:10.1038/350039a0
- 480 Masuda, K., Nishizawa, O., Kusunose, K., Satoh, T., Takahashi, M., & Kranz, R. L. (1990).  
481 Positive feedback fracture process induced by nonuniform high-pressure water flow in  
482 dilatant granite, *Journal of Geophysical Research*, 95(B13), 21,583–21,592, doi:10.1029/  
483 JB095iB13p21583
- 484 Masuda, K., Nishizawa, O., Kusunose, K., & Satoh, T. (1993). Laboratory study of effects  
485 of in situ stress state and strength on fluid-induced seismicity, *International Journal of*  
486 *Rock Mechanics and Mining Sciences & Geomechanics Abstracts*, 30, 1-10,  
487 [http://dx.doi.org/10.1016/0148-9062\(93\)90171-9](http://dx.doi.org/10.1016/0148-9062(93)90171-9)
- 488 Masuda, K., Arai, T., Fujimoto, K., Takahashi, M., & Shigematsu, N. (2012). Effect of

- 489 water on weakening preceding rupture of laboratory-scale faults: Implications for long-  
 490 term weakening of crustal faults, *Geophysical Research Letters*, 39, L01307,  
 491 doi:10.1029/2011GL050493
- 492 Masuda, K. (2013). Source duration of stress and water-pressure induced seismicity derived from  
 493 experimental analysis of P wave pulse width in granite. *Geophysical Research Letters*,  
 494 40, 3567-3571, DOI: 10.1002/grl.50691
- 495 Masuda, K., Satoh, T., & Nishizawa, O. (2013). Ultrasonic transmission and acoustic emission  
 496 monitoring of injection-induced fracture processes in rock samples, *Proceedings of the*  
 497 *47th US Rock Mechanics/Geomechanics Symposium 23-26 June 2013*, San Francisco,  
 498 California, USA, ARMA13-295
- 499 Mavko, G., Mukerji, T., & Dvorkin, J. (2009). *The rock physics handbook*, 2nd ed.,  
 500 UK: Cambridge Univ. Press.
- 501 Meglis, I. L., Greenfield, R. J., Engelder, T., & Graham, E. K. (1996). Pressure  
 502 dependence of velocity and attenuation and its relationship to crack closure in  
 503 crystalline rocks, *Journal of Geophysical Research*, 101(B8), 17,523–17,533,  
 504 doi:10.1029/96JB00107
- 505 Moore, D. E., & Lockner, D. A. (1995). The role of microcracking in shear-fracture  
 506 propagation in granite, *Journal of Structural Geology*, 17, 95–114,  
 507 [http://dx.doi.org/10.1016/0191-8141\(94\)E0018-T](http://dx.doi.org/10.1016/0191-8141(94)E0018-T)
- 508 Nishizawa, O., & Masuda, K. (1991). Characterization of microcracks estimated from  
 509 P-wave velocity change caused by high-pressure water flow in dilatant granite,  
 510 *Geophysical Exploration (Butsuri-tansa)*, 44, 255-265 (in Japanese with English  
 511 abstract)
- 512 O'Connell, R. J., & Budiansky, B. (1974). Seismic velocities in dry and saturated  
 513 cracked solids, *Journal of Geophysical Research*, 79(35), 5412–5426,  
 514 doi:10.1029/JB079i035p05412
- 515 Ohtake, M. (1987). Temporal change of  $Q_p^{-1}$  in focal area of 1984 western Nagano,  
 516 Japan, earthquake as derived from pulse width analysis, *Journal of Geophysical*  
 517 *Research*, 92(B6), 4846–4852, doi:10.1029/JB092iB06p04846
- 518 Paterson, M. S., & Wong, T-F. (2005). *Experimental rock deformation – The brittle*  
 519 *field*, 2nd ed., NY, Springer.
- 520 Prioul, R., Cornet, F. H., Dorbath, C., Dorbath, L., Ogena, M., & Ramos, E. (2000). An  
 521 induced seismicity experiment across a creeping segment of the Philippine Fault,  
 522 *Journal of Geophysical Research*, 105(B6), 13,595–13,612, doi:10.1029/2000JB900052
- 523 Raleigh, C. B., Healy, J. H., & Bredehoeft, J. D. (1976). An experiment in earthquake  
 524 control at Rangely, Colorado, *Science*, 191, 1230–1237,  
 525 doi:10.1126/science.191.4233.1230, doi:10.1126/science.191.4233.1230
- 526 Rutqvist, J., Birkholzer, J. T., & Tsang, C.-F. (2008). Coupled reservoir–geomechanical  
 527 analysis of the potential for tensile and shear failure associated with CO<sub>2</sub> injection in  
 528 multilayered reservoir–caprock systems, *International Journal of Rock Mechanics and*  
 529 *Mining Sciences*, 45, 132–143, <http://dx.doi.org/10.1016/j.ijrmms.2007.04.006>
- 530 Scholz, C. H. (1968), Experimental study of the fracturing process in brittle rock, *Journal of*  
 531 *Geophysical Research*, 73(4), 1447–1454, doi:10.1029/JB073i004p01447
- 532 Scholz, C. H., (2002), *The mechanics of earthquakes and faulting*, 2nd ed., UK: Cambridge  
 533 Univ. Press.
- 534 Schön, J. H., (2011), *Physical properties of rocks: A Workbook, Handbook of Petroleum*

- 535 *Exploration and Production*, 8, GB, Elsevier.
- 536 Schubnel, A., Nishizawa, O., Masuda, K., Lei, X., Xue, Z., & Guégen, Y. (2003).  
537 Velocity measurements and crack density determination during wet triaxial experiments  
538 on Oshima and Toki granites, *Pure and Applied Geophysics*, 160, 869-887, doi:10.1007/  
539 PL00012570
- 540 Schultz, R., Wang, R., Gu, Y. J., Haug, K. & Atkinson, G. (2017). A seismological overview of  
541 the induced earthquakes in the Duvernay play near Fox Creek, Alberta, *Journal of*  
542 *Geophysical Research: Solid Earth*, 122, 492–505. doi:10.1002/2016JB013570
- 543 Schultz, R., Atkinson, G., Eaton, D. W., Gu, Y. J., & Kao, H. (2018). Hydraulic fracturing  
544 volume is associated with induced earthquake productivity in the Duvernay play. *Science*  
545 359 (6373), 304-308. DOI: 10.1126/science.aao0159
- 546 Schultz, R., Skoumal, R. J., Brudzinski, M. R., Eaton, D., Baptie, B., & Ellsworth, W. (2020).  
547 Hydraulic fracturing–induced seismicity. *Reviews of Geophysics*, 58, e2019RG000695.  
548 <https://doi.org/10.1029/2019RG000695>
- 549 Soga, N., Mizutani, H., Spetzler, H., & Martin III, R. J. (1978). The effect of dilatancy  
550 on velocity anisotropy in Westerly granite, *Journal of Geophysical Research*, 83(B9),  
551 4451–4458, doi:10.1029/JB083iB09p04451
- 552 Stanchits, S., Mayr, S., Shapiro, S., & Dresen, G. (2011). Fracturing of porous rock  
553 induced by fluid injection, *Tectonophysics*, 503, 129-145,  
554 <http://dx.doi.org/10.1016/j.tecto.2010.09.022>
- 555 Wang, Z., Lei, X., Ma, S., Wang, X., & Wan, Y. (2020). Induced earthquakes before and after  
556 cessation of long–term injections in Rongchang gas field. *Geophysical Research Letters*,  
557 47, e2020GL089569. <https://doi.org/10.1029/2020GL089569>
- 558 Wong, T.-F. (1982). Micromechanics of faulting in Westerly granite, *International Journal of*  
559 *Rock Mechanics and Mining Sciences & Geomechanics Abstracts*, 19, 49–64,  
560 [http://dx.doi.org/10.1016/0148-9062\(82\)91631-X](http://dx.doi.org/10.1016/0148-9062(82)91631-X)
- 561 Zoback, M. D., & Harjes, H.-P. (1997). Injection-induced earthquakes and crustal stress  
562 at 9 km depth at the KTB deep drilling site, Germany, *Journal of Geophysical Research*,  
563 102(B8), 18,477–18,491, doi:10.1029/96JB02814
- 564